Magnetically Actuated Fiber-Based Soft Robots

Youngbin Lee, Florian Koehler, Tom Dillon, Gabriel Loke, Yoonho Kim, Juliette Marion, Marc-Joseph Antonini, Indie C. Garwood, Atharva Sahasrabudhe, Keisuke Nagao, Xuanhe Zhao, Yoel Fink, Ellen T. Roche, and Polina Anikeeva*

Broad adoption of magnetic soft robotics is hampered by the sophisticated field paradigms for their manipulation and the complexities in controlling multiple devices. Furthermore, high-throughput fabrication of such devices across spatial scales remains challenging. Here, advances in fiber-based actuators and magnetic elastomer composites are leveraged to create 3D magnetic soft robots controlled by unidirectional fields. Thermally drawn elastomeric fibers are instrumented with a magnetic composite synthesized to withstand strains exceeding 600%. A combination of strain and magnetization engineering in these fibers enables programming of 3D robots capable of crawling or walking in magnetic fields orthogonal to the plane of motion. Magnetic robots act as cargo carriers, and multiple robots can be controlled simultaneously and in opposing directions using a single stationary electromagnet. The scalable approach to fabrication and control of magnetic soft robots invites their future applications in constrained environments where complex fields cannot be readily deployed.

1. Introduction

Soft robotic systems have garnered significant interest for their promise in biomedical applications ranging from prosthetics to minimally-invasive surgery.[1,2] Among stimuli used to actuate soft robots,[3] magnetic fields offer advantages over pressure,[4,5] light,[6,7] heat,[6,8–10] or electric fields.[11,12] First, magnetically-actuated robots can be deployed untethered.[13–15] Second, weak magnetic fields (<50 mT) penetrate deep into non-magnetic and weakly-conductive media, such as biological matter, making them particularly attractive signals in biomedical contexts.[16] These advantages have inspired a wealth of magnetic soft robotics research with applications in surgery,[17,18] biopsy,[19,20] and drug delivery.[21–23]

Despite their technological promise, the broad deployment of magnetically-actuated soft robotics remains hindered

Y. Lee, G. Loke, J. Marion, K. Nagao, Y. Fink, P. Anikeeva
Department of Materials Science and Engineering
Massachusetts Institute of Technology
Cambridge, MA 02139, USA
E-mail: anikeeva@mit.edu

Y. Lee, F. Koehler, G. Loke, J. Marion, M.-J. Antonini, A. Sahasrabudhe,
K. Nagao, Y. Fink, P. Anikeeva
Research Laboratory of Electronics
Massachusetts Institute of Technology
Cambridge, MA 02139, USA

F. Koehler
Department of Electrical Engineering and Computer Science
Massachusetts Institute of Technology
Cambridge, MA 02139, USA

T. Dillon, Y. Kim, X. Zhao, E. T. Roche
Department of Mechanical Engineering
Massachusetts Institute of Technology
Cambridge, MA 02139, USA

I. C. Garwood
Harvard/MIT Health Science & Technology Graduate Program
Cambridge, MA 02139, USA

A. Sahasrabudhe, P. Anikeeva
McGovern Institute for Brain Research
Massachusetts Institute of Technology
Cambridge, MA 02139, USA

A. Sahasrabudhe
Department of Chemistry
Massachusetts Institute of Technology
Cambridge, MA 02139, USA

X. Zhao
Department of Civil and Environmental Engineering
Massachusetts Institute of Technology
Cambridge, MA 02139, USA

Y. Fink
Institute for Soldier Nanotechnologies
Massachusetts Institute of Technology
Cambridge, MA 02139, USA

E. T. Roche
Institute for Medical Engineering and Science
Massachusetts Institute of Technology
Cambridge, MA 02139, USA

P. Anikeeva
Department of Brain and Cognitive Sciences
Massachusetts Institute of Technology
Cambridge, MA 02139, USA

**ADVANCED
SCIENCE NEWS**

www.advancedsciencenews.com

**ADVANCED
MATERIALS**

www.advmat.de

by challenges in their fabrication and control. To date, magnetic soft robots are predominantly 2D structures fabricated by molding[24–26] or stereolithographic processes.[27–29] The demand for increased functionality, however, necessitates more complex 3D architectures. Although micro-assembly from molded building blocks[30–32] and 3D printing with multiple photolithographic steps[33,34] can yield 3D actuators, these processes are labor-intensive and offer limited scalability. Additional stimuli such as light can be leveraged to transform 2D structures into 3D magnetic robots,[23] but the necessity of dual signals increases the complexity of the robot control and reduces the working distance for remote operation in non-transparent matter. In addition to the challenges in their scalable fabrication, magnetic soft robotics currently rely on complex multidirectional or rotating magnetic fields for their actuation.[23,24,26–30] The ability to produce and control magnetic fields in 3D demands sophisticated and bulky apparatuses consisting of multiple magnets or electromagnetic coils, which further restrict the working volumes.[15] Finally, precise tailoring of magnetic field profiles to the robot geometry has so far necessitated that in a given field all deployed robots move in the same direction. Taken together, innovation in fabrication methods for complex architectures and the simplification of magnetic control schemes may enhance the utility of magnetic soft robots and broaden their adoption in biomedical and engineering applications.

Here, magnetic soft robots were created by combining fiber-based fabrication and mechanical and magnetic programming for locomotion under weak unidirectional magnetic fields. The elastomeric fibers produced via thermal drawing at a scale of hundreds of meters were instrumented with stretchable ferromagnetic composite and then subjected to a macroscale strain treatment to transform them into helical structures.[9,35] By varying the strain and magnetization treatment, worm-like crawlers and bipedal walkers were engineered. Their locomotion as well as payload delivery was then achieved in unidirectional magnetic fields orthogonal to the plane of motion. We anticipate that scalable fabrication and strain engineering in elastomeric fibers will expand the range of architectures of magnetic soft robots, while their control with stationary electromagnets paves the way to their applications in spatially constrained biomedical and engineering contexts.

2. Results

To produce 3D magnetically-actuated robots, we have leveraged thermal drawing and strain engineering that have enabled thermal actuation of fiber-based artificial muscles[9] and hypothesized that the introduction of permanently magnetized elements into the fiber-based actuators would enable their remote control via magnetic fields. To create fibers compatible with the introduction of magnetic actuation elements, we first thermally drawn from macroscale preforms, bimorph structures of styrene-ethylene-butylene-styrene (SEBS) and cyclic olefin copolymer elastomer (COCe); these structures also included a hollow channel (**Figure 1**a,b). The fiber volume fraction of the hollow channel was 36%–40% to enable effective magnetic actuation following the introduction of a ferromagnetic composite. As SEBS and COCe are elastomers, their bimorphs were embedded within a thermoplastic poly(methyl methacrylate) (PMMA) cladding dur-

ing drawing, which was then mechanically stripped. SEBS and COCe were selected for their similar drawing temperature,[36,37] low modulus (Table S1, Supporting Information), and biochemical inertness.[38,39] Additionally, SEBS and COCe exhibit different elongation at break (ϵ_{max}) (Table S1, Supporting Information), which implies that under tensile stress COCe undergoes greater plastic deformation than SEBS. Consequently, upon release the greater permanent elongation in COCe yields excess tensile stress in SEBS, which can be accommodated via formation of helices.[9] To facilitate helix formation in a pre-determined direction, cross-sectional asymmetry of the COCe layer and microfluidic channel placement was introduced into the bimorph fiber architectures (Figure 1b and Note S1, Supporting Information). Fibers retained cross-sectional architectures of the preforms with the reduction ratios of 20 or 40 (Figure 1c,d), and their dimensions could be tuned between 1000×500 (R20) and $500 \times 200 \ \mu m^2$ (R40)[35] (Figure S1, Supporting Information).

To magnetically actuate thermally drawn fibers, we sought to fill their hollow channels with a ferromagnetic composite. The target composite had to exhibit programmable magnetization, be compatible with the injection into the fibers, ensure strong adhesion to SEBS, exhibit mechanical moduli comparable to SEBS and COCe, and be able to withstand strains in the range of 250%–400% necessary for the formation of fiber-based helical actuators. Ferromagnetic neodymium–iron–boron ($Nd_2Fe_{14}B$) alloy particles were selected as a magnetic component for fiber actuation due to their high coercivity (0.92 T) and remanence (0.85 T) compared to those of other common magnetic materials, such as Fe_3O_4 and Sm_2Co_{17}.[40,41] In a non-magnetized state, the particles exhibit a multi-domain ferromagnetic order with zero net magnetization, which enables their dispersion in polymer matrices. The application of a magnetic field above the coercive field permanently magnetizes the particles endowing elements of the fiber with magnetic moments that could be manipulated via a weak magnetic field.[22]

To meet the injection, flexibility, stretchability, and adhesion requirements of the composite, we engineered a photo-curable elastomer with low viscosity prior to crosslinking. A photo-curable matrix was chosen for its rapid cross-linking that ensured a uniform distribution of magnetic particles (MPs) that may precipitate in low-viscosity media (Figure 1e).

Thiol-ene chemistry has been extensively applied to the design of photo-curable polymers with widely ranging mechanical and thermal properties.[42] To create an elastomer with mechanical properties comparable to SEBS and COCe, we combined a dialkene tri(ethylene glycol) divinyl ether (TEGDVE, 2A) with mixtures of a dithiol 2,2'-(ethylenedioxy)diethanethiol (EDDET, 2T) and a tetrathiol pentaerythritol tetrakis(3-mercaptopropionate) (PETMP, 4T). TEGDVE and PETMP have been previously shown to photo-crosslink into flexible networks, but due to the high density of crosslinks formed by PETMP their peak strain (9.3%) was far below the strains necessary for the formation of helical actuators.[43] Ether linkages[44] and dithiol groups of EDDET enable long, flexible linear chain formation between crosslinks following its polymerization with TEGDVE. The molar ratio of PETMP and EDDET then controls the extension properties of the $4T_x2T_{1-x}2A$ polymer networks. The fraction x = 0.04 of PETMP was found to yield polymer networks ($4T_42T_{96}2A_{100}$) with the highest ϵ_{max} (478.5%) as compared to other compositions and
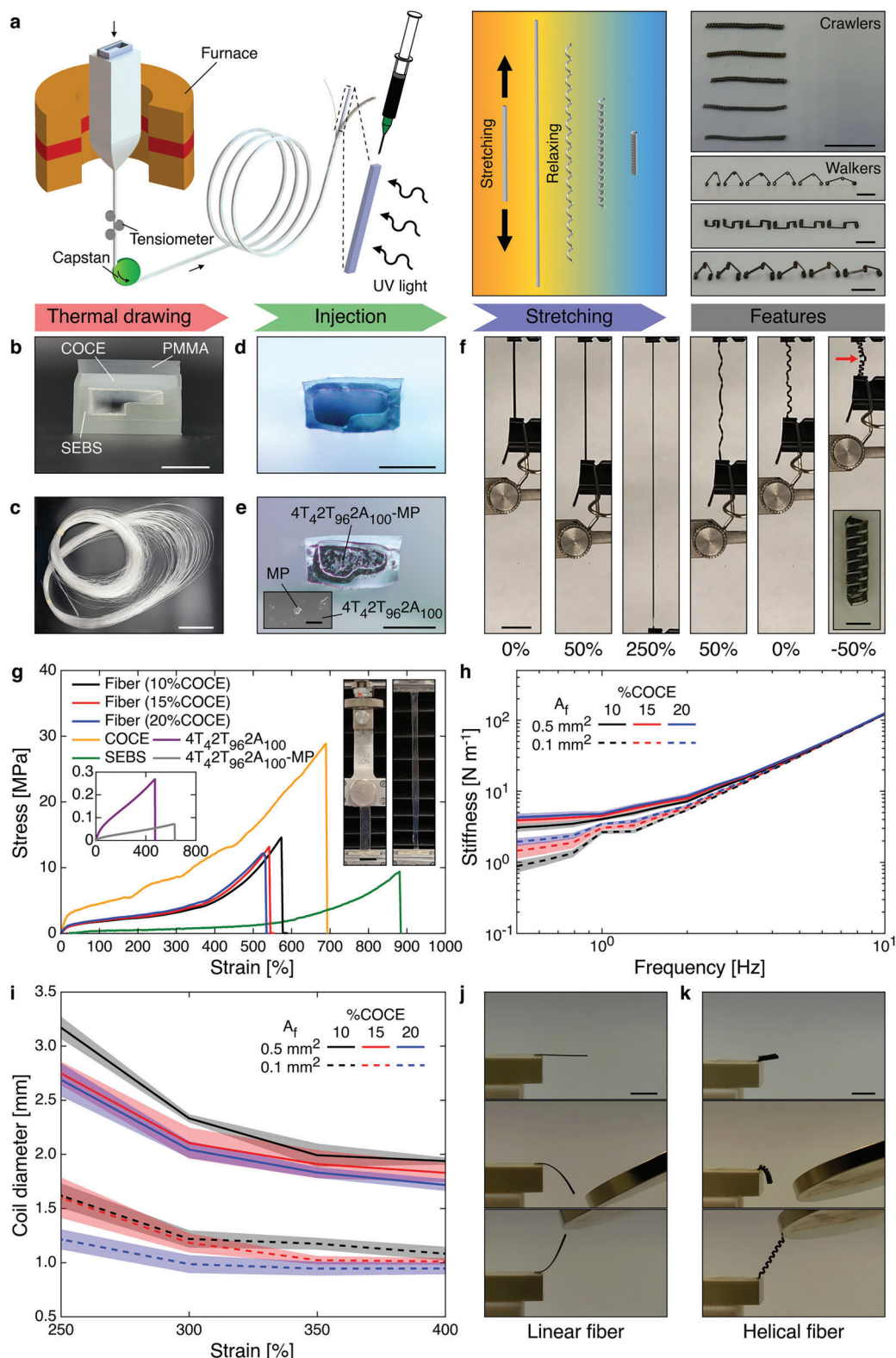
Figure 1. Fabrication and characterization of magnetically-actuated fibers. a) Schematic of the fabrication process of 3D fiber-based magnetic soft robots. Scale bars represent 1 cm. b) Cross-sectional image of the preform. Scale bar represents 1 cm. c) Bundles of thermally drawn fibers. The scale bar represents 10 cm. d) Cross-sectional image of thermally drawn fiber following the removal of the PMMA cladding. Scale bar represents 500 μm. e) Cross-sectional image of a fiber following injection and photo-curing of the magnetic composite. Scale bar represents 500 μm. The inset shows an SEM image of NdFeB particles embedded in $4T_42T_{96}2A_{100}$ polymer and the scale bar is 20 μm. f) Pictures of strain engineering process to create the helical

ADVANCED
SCIENCE NEWS

www.advancedsciencenews.com

**ADVANCED
MATERIALS**

www.advmat.de

hence was selected for the magnetic composites (Table S2, Supporting Information). The addition of MPs at 33.3 wt% resulted in an increase in the maximum elongation to 618.9% likely due to the reduction in UV light penetration, and thus the degree of photo-crosslinking in the polymer matrix. The composite of $4T_4 2T_{96} 2A_{100}$ and MPs ($4T_4 2T_{96} 2A_{100}$-MP) maintained stable interfaces with SEBS under a tensile strain of 400% due to their adhesive interaction (Figure S2, Supporting Information).

To produce magnetic soft robots with helical domains, fibers injected with the $4T_4 2T_{96} 2A_{100}$-MP were photo-cured and subjected to strains between 250% and 400% (Figure 1f and Movie S1, Supporting Information). The formation of helical domains was often accompanied by the emergence of unstable bifurcations, termed perversions.[9] These perversions were eliminated by rewinding the fibers in one direction following the formation of helical domains (Figure S3, Supporting Information).

We reasoned that the mechanical properties of the fibers would determine the responsiveness of the fiber-based robots. Consistent with the greater modulus of COCe as compared to SEBS, increasing the COCe content (from 10 to 20 vol%) in the bimorph fibers resulted in a lower ϵ_{max} (Figure 1g) and a higher bending stiffness of the devices (Figure 1h).

A higher fraction of COCe and a larger applied strain led to helices with greater density and lower diameter of the turns to accommodate higher strain energies[9] (Figure 1i). Therefore, by controlling the COCe composition, fiber size, and strain, mechanical properties and dimensions of the fiber-based structures can be tuned. Exposing the fibers filled with $4T_4 2T_{96} 2A_{100}$-MP to a high magnetizing field then permits their manipulation with weak magnetic fields (Figure 1j,k and Movie S2, Supporting Information).

By engineering helical domains into the fibers, we demonstrate two types of magnetically-controlled locomotion (**Figure 2**). Continuous helical structures were designed to mimic the crawling motion inspired by caterpillars (Figure 2a). However, in contrast to prior work that relied on folding at a single point,[45,46] we hypothesized that folding at two points would introduce asymmetry and enable movement under unidirectional magnetic fields. Helical architectures are expected to require reduced forces necessary for folding as compared to similarly sized linear structures, as well as to increase the contact area with the ground ensuring directional stability during locomotion.

To achieve double folding and forward crawling under unidirectional fields orthogonal to the plane of motion (z-direction), the helical structures were magnetized to establish 5 magnetic domains (Figure 2a). Application of a z-directional field yields alignment of "head", "body", and "tail" domains, and the resulting forces manifest in folding. This domain structure was established by designing alignment fixtures that helical fibers were affixed to during magnetization (Figure 2b). A magnetizing field, which exceeded the coercivity field of the MPs, resulted in their permanent magnetization in the direction of the field, which then remained following the release of the crawlers from the alignment fixtures.

To mimic bipedal walking, helical structures were introduced into three partial sections of linear fibers for two "foot" helices and a joint helix (Figure 2c). The foot helices permitted engineering of the robot contact area with the surface, while the flexible joint coil ensured the ability to impart large differences in magnetization direction between the legs. We hypothesized that introducing asymmetry into the leg length and foot width would prescribe the direction of locomotion under a unidirectional field (see Experimental Section for fabrication details).

To enable folding at the joint and hence walking motion in the z-directional magnetic field, magnetic domains were introduced into the walkers via exposure to a magnetizing field while the structures were affixed to alignment fixtures (Figure 2d). To investigate the effects of geometry on locomotion, an array of alignment fixtures was implemented to vary the magnetization angles for the short ($\theta_{M,S}$) and the long ($\theta_{M,L}$) legs. While the values of $\theta_{M,S}$ were motivated by the need to maximize the magnetic force in the shorter (stiffer) leg, the range of $\theta_{M,L}$ was constrained by structural limitations. Varying the initial joint angles (θ_J) allowed for additional tunability in the relative leg magnetization directions for a given set of $\theta_{M,S}$ and $\theta_{M,L}$ used during magnetization process.

To evoke linear motion in crawlers, these devices were exposed to a z-directional magnetic field sinusoidally varying in time between 0 and 45 mT at frequencies up to 10 Hz (**Figure 3**a and Movie S3, Supporting Information). When the magnetic field increases, the attraction between the head, body, and tail domains yields double folding and introduces strain into the structure (Figure S4, Supporting Information). The crawler has two points of contact with the ground, one in the head and one in the tail domain. To elicit forward motion, the friction at the head should exceed the friction at the tail during folding, while friction at the tail should exceed the friction at the head during unfolding.

To maximize the degree of folding under a magnetic field, a fiber with the lowest bending stiffness (R40, 10%COCe) was selected. As bending stiffness of helices decreases with the increasing coil diameter (D_C),[47] larger coils ($D_C = 1.22$ mm) were introduced into fibers via a relatively low 290% strain. Using these fibers, we investigated the role of the magnetization configuration (as defined by body length (L_B), tail length (L_T), head curvature (R_H), and tail curvature (R_T), Figure 2b) on the crawling efficacy.

At the fixed R_H and R_T (1.5 mm), increasing L_T as compared to L_B increases the friction at the tail, which interferes with

---

structure from an as-drawn fiber. The red arrow indicates a perversion. The scale bar represents 1 cm. The inset shows the helical fiber after removal of the perversion and its scale bar is 1 mm in length. g) Stress–strain curves of the fibers and individual components. The black, red, and blue lines indicate 10, 15, and 20%COCe integrated fibers with magnetic composite, respectively. Orange, green, purple, and gray lines represent COCe, SEBS, polymer matrix, and magnetic composite, respectively. The inset shows the elongation of the $4T_4 2T_{96} 2A_{100}$ polymer under 250% tensile strain and its scale bar is 1 cm in length. h) Measured bending stiffness for fibers with various compositions and sizes. The black, red, and blue curves represent the stiffness of 10, 15, and 20% COCe fibers, respectively. Solid and dashed lines indicate fibers with cross-sectional area of 0.5 and 0.1 mm², respectively. Shaded areas correspond to the standard errors (n=5 samples). i) Coil diameters of the helical fibers depending on compositions, sizes, and strain. The black, red, and blue curves indicate the coil diameters of 10, 15, and 20%COCe fibers, respectively. Solid and dashed lines represent fibers with cross-sectional area of 0.5 and 0.1 mm², respectively. Shaded areas show standard deviations (n=5 samples). j,k) Magnetic actuation of (j) linear and (k) helical fibers using a permanent magnet. Scale bars represent 1 cm.

**ADVANCED
SCIENCE NEWS**

www.advancedsciencenews.com

**ADVANCED
MATERIALS**

www.advmat.de
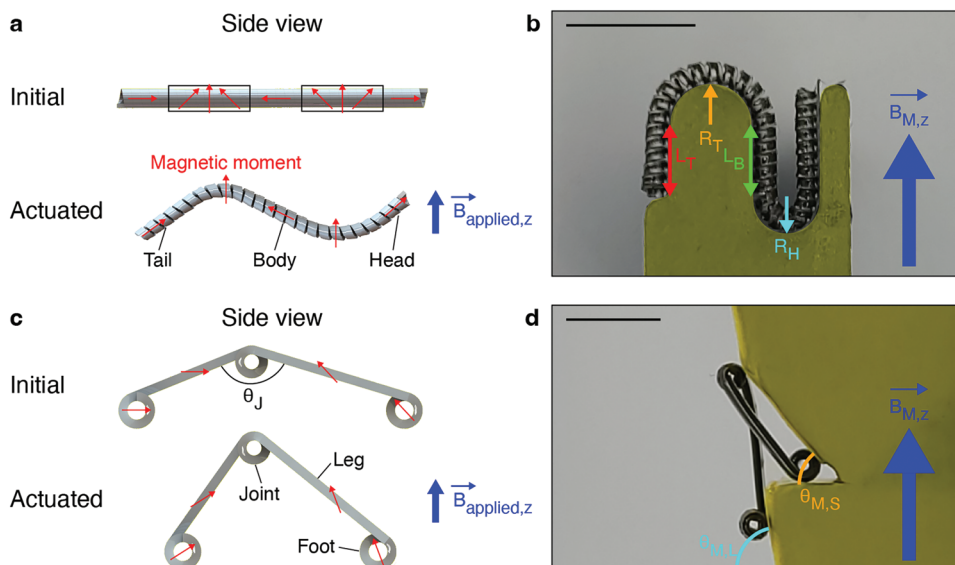
Figure 2. Structural and magnetic properties of 3D magnetic soft robots. a,c) Schematic of (a) the crawler and (c) the walker at the initial and actuated states. Red arrows indicate the expected magnetic moment direction following magnetization. The magnetic field actuating the robot is applied along the direction of the blue arrow. b,d) Positions of (b) the crawler and (d) the walker on their alignment fixtures (in yellow) during magnetization. (b) The colored arrows indicate defining the length parameters for crawlers and (d) the colored arcs indicate defining the magnetization angle parameters for walkers. The external magnetizing field is applied along the direction of the blue arrow. Scale bars are 5 mm.

forward movement (Figure 3b). However, shortening $L_T < 1.5$ mm results in insufficient friction at the tail during unfolding, leading to a stationary crawler. Increasing both L_T and L_B decreases the elastic recovery force necessary to observe motion. For the fixed L_B and L_T (3.0 mm) increasing R_H as compared to R_T has negligible influence on crawling motion, whereas crawlers with large R_T exhibit similar behaviors to those with simultaneously increased L_B and L_T (Figure 3c). The range of parameters enabling locomotion narrows for crawlers with smaller D_C values due to their increased stiffness (Figure S5, Supporting Information).

By varying the frequency of the oscillating field (Figure 3d), the number of folding cycles and the crawling velocity can be increased. However, the friction and viscous lag in folding and unfolding yield lower degree of compression at higher frequencies, which leads to a plateau in crawling velocity beyond 3 Hz. Additionally, slip is observed more readily at higher frequencies, which manifests in large deviations in the velocity.

We tested the ability of the crawlers to carry cargo in their head compartments (Figure 3e and Movie S4, Supporting Information). To account for the additional weight of the head, L_B of the cargo carrying crawlers was increased to avoid higher friction at the tail at the initiation of folding due to the slower motion of the head. The release of the cargo was accomplished by switching the direction of the magnetic field, which resulted in the reversal of the head domain (Figure 3f and Movie S4, Supporting Information).

Bipedal locomotion of magnetic walkers was demonstrated under unidirectional magnetic fields (Movies S5 and S6, Supporting Information). However, rather than applying a sinusoidal wave, the same electromagnet delivered a sawtooth wave with the field increasing from 0 to 23–25 mT in the first 80% of a period τ followed by a sharp drop back to 0 mT allowing for a rapid release

of the elastic energy in each step (**Figure 4**a). The asymmetry in the leg length of walkers enabled deterministic control over their walking direction toward the longer leg (LLD) or the shorter leg (SLD) using fabrication parameters (θ_J, $\theta_{M,L}$, and $\theta_{M,S}$, Figure 4b). In both modes, during the gradual increase in the field strength, the front foot remains stationary, while the back foot slides forward due to the alignment of magnetic moments to an external field. During recovery, the back foot is stationary, and the front foot is propelled forward as the elastic energy stored in the fiber is released. To overcome the friction at the front foot during recovery, a walker capable of storing a higher elastic energy is advantageous, and hence the fibers with higher bending stiffness (R20, 20%COCe) were selected (Figure 1h).

We applied a hybrid statics-dynamics model to predict the direction of motion of asymmetric walkers with different geometries (Figure 4b and Note S2, Supporting Information). In qualitative agreement with predictions, $\theta_J < 107°$ favored LLD movement regardless of the leg magnetization angles in experimentally produced walkers. Reduced friction on the short leg due to the decrease in the ratio of normal to tangential forces increased the likelihood of the short leg slip upon magnetic field application. In contrast, at $\theta_J > 107°$, small $\theta_{M,L}$, greater alignment of the long-leg magnetization with the magnetic field, and a reduced long-leg torque permitted SLD movement. For large $\theta_{M,L}$ and $\theta_J > 107°$, the walkers' folding and unfolding motions are in the opposite directions, and the prediction of net motion offers limited confidence (the purple regions in Figure 4b). Experimental results suggest that walking can occur in either direction in this regime, which may be attributed to the degree of motion during folding and unfolding. In the future, combined modeling of magnetic, elastic, and frictional forces will offer additional insights into actuating mechanism in this system and facilitate development of more complex modes of actuation.[22,23,29,48]
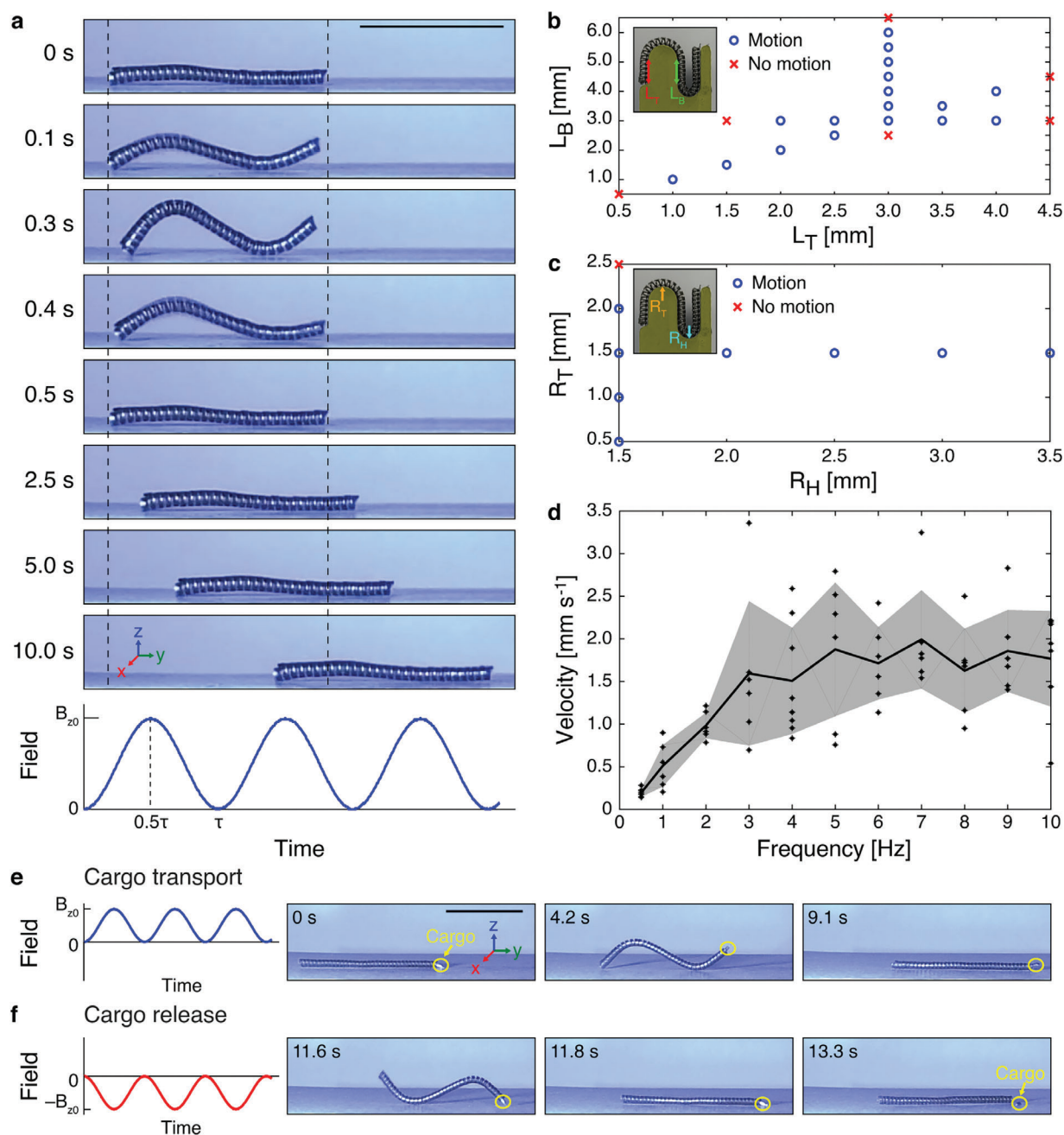
Figure 3. Crawling motion of 3D magnetic soft robots. a) Photographs of the left-to-right motion of the crawler under an oscillating, unidirectional, sinusoidal 2 Hz magnetic field along the z-direction. The scale bar is 1 cm. b,c) Motility study of the crawler depending on (b) length and (c) curvature magnetization parameters (see insets). Blue circle and red cross represent motion and no motion, respectively. d) Measured crawling velocity in y-direction depending on the magnetic field frequency. Black line and shaded area present the mean and standard deviation of the crawling velocity, respectively (n ≥ 5 samples). e,f) Photographs of a crawler used as a cargo carrier. The cargo is circled in yellow. The magnitude of the magnetic fields applied along the z-direction for transporting (e) and releasing (f) modes are plotted on the left. Scale bar = 1 cm. All crawler parameters are summarized in Table S3 (Supporting Information).

Introducing 1–2 additional turns into the back-foot helix as compared the front foot increases the back-foot friction and reduces the likelihood of slip manifesting in more consistent stepping motion (Figure 4c). Adding more than two additional turns into the back-foot helix, however, yields excess friction and back-leg pinning.

The velocity of walkers in both modes increases with the frequency of the magnetic field prior to reaching a peak at 7 Hz (Figure 4d). Akin to the crawling motion, the degree of actuation is reduced at higher frequencies. Additionally, a greater probability of the back-foot slip leads to large deviations in velocity at higher frequencies.
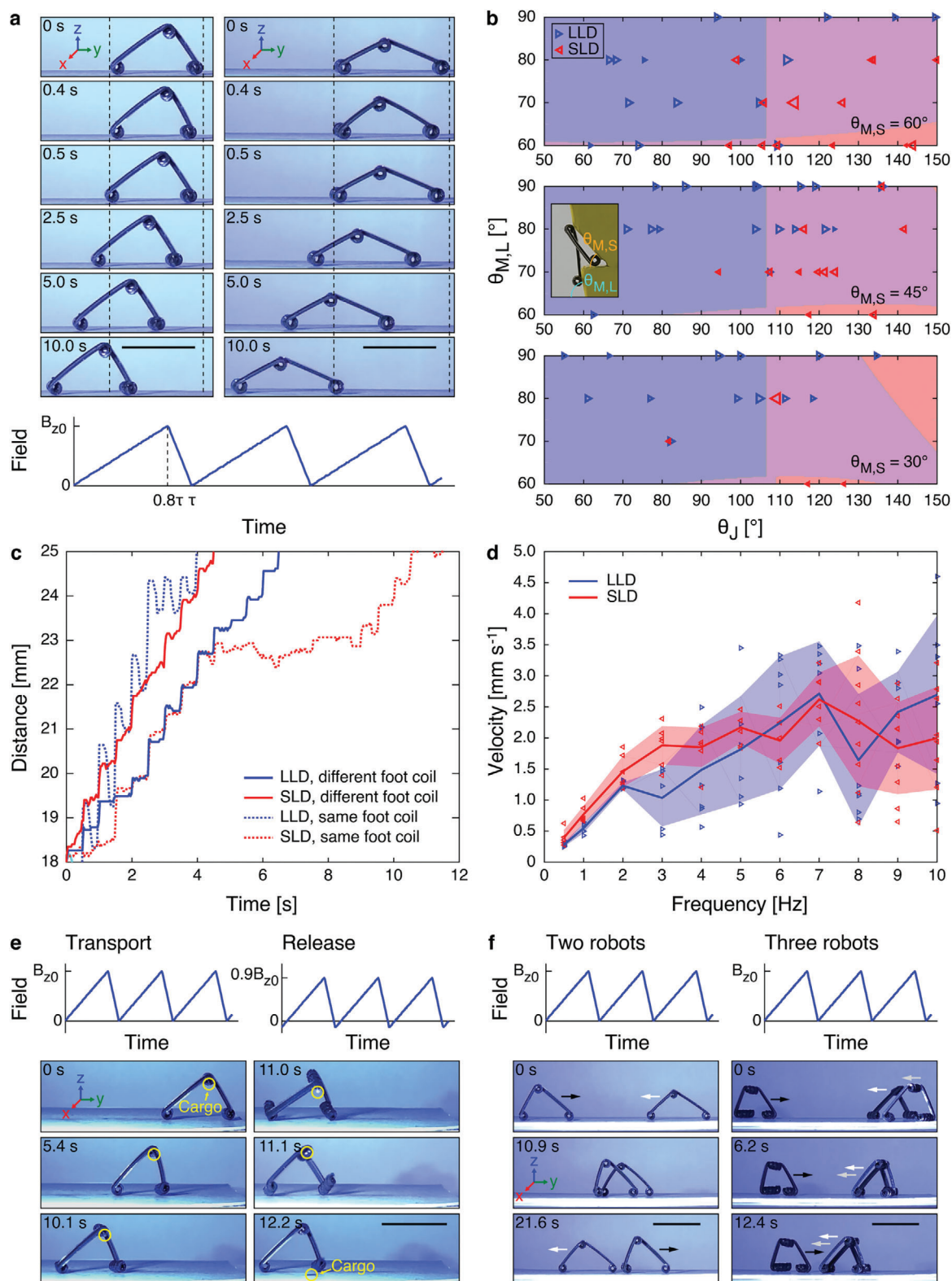
Figure 4. Walking motion of 3D magnetic soft robots. a) Photographs of the right-to-left motion of two walkers under a 2 Hz oscillating, unidirectional sawtooth magnetic field. Each walker has different coil numbers at each foot (different foot coil condition). Scale bars represent 1 cm. b) Relationship between the angle parameters (see inset) and motility of the walker, which has the same coil number in their feet (same foot coil condition). Blue and red triangles represent LLD (long-leg direction) and SLD (short-leg direction) walking motion, respectively. Triangle size is proportional to the walking velocities. The blue and red shaded areas represent direction of motion as predicted by a hybrid statics-dynamics model; blue and red correspond

Walkers were evaluated for their ability to carry cargo within their joint coil compartments (Figure 4e and Movie S7, Supporting Information). In contrast to crawlers, the cargo weight has limited effect on the walking motion since there is no actuation at the joint. To release the cargo, magnetic field direction can be briefly reversed. This triggers an attempt in magnetization reversal in the legs, which would yield walker inversion. Offsetting the magnetic field stimulus by -3.6 mT yields brief 0.13τ epochs of attempted magnetization reversal manifesting in oscillatory shaking motion, which enables cargo release.

Finally, taking advantage of the programmable motion direction and velocity, multiple walkers can be controlled to travel in different directions under a single unidirectional field (Figure 4f and Movies S8 and S9, Supporting Information). This enables directing multiple cargo-carrying walkers to spatially distinct targets simultaneously.

3. Conclusion

In this work, a combination of magnetic composite engineering, high-throughput fiber fabrication, and macroscale strain and magnetization programming enabled scalable production of 3D magnetic soft robots controllable by unidirectional magnetic fields applied via stationary electromagnets. SEBS and COCe were selected for the bimorphic elastomeric fibers based on their similar drawing conditions, low modulus, and differing yield strains. Tuning the fraction of stiffer, less stretchable COCe permitted modulation of mechanical properties the fiber robots and their responses to magnetic fields.

Although here we focused on two types of locomotion, spatially restricted strain to form helical joints may enable more complex architectures as well as additional forms of locomotion such as swimming (Movie S10, Supporting Information). Additionally, it was our goal to demonstrate locomotion with structures engineered from fibers processed in a high-throughput manner, consequently we purposefully avoided further modification of these devices following application of strain. It is, however, expected that surface treatments aimed at modulating friction localized to specific points could further improve the device performance.[49]

As fibers are typically drawn at 100–1000 s m scales, each fiber can deliver thousands of soft magnetically-actuated structures with programmable locomotion. In the current work, we sought to investigate the parameter space of the fiber-based robots and, consequently, the fibers were subjected to strain individually. However, for a fixed architecture, multiple robots can be manufactured at scale. For instance, following thermal drawing, magnetic composite can be injected into two-meter sections of fiber. Multiple magnetic fiber sections could be stretched via a wide clamp, and multiple robots could be magnetized in a large-volume electromagnet. Furthermore, over 1000 soft robots could be fabricated in a single step via thermal drawing with composite injection[50] and strain engineering in series.[51]

Here we focused on fibers with cross-sectional dimensions 0.1–0.5 mm², however, the fiber drawing process readily delivers structures with linear dimensions ≤10 µm compatible with actuation.[9] In addition, fiber fabrication lends itself to incorporation of functional features such as conductive elements[50,52] or solid-state microdevices[51,53] that may further enhance the utility of fiber-based robots.

We demonstrated that helical compartments within the magnetic fiber-based robots could store cargo, which could be released by simple switching of the magnetic field parameters of a unidirectional magnetic field generated by the same electromagnet as used to drive locomotion. Notably, simultaneous control of multiple robots moving in different direction was possible using a single electromagnet.

Given their tunable materials properties, dimensions, and locomotion modalities these devices may impact applications in soft robotics and biomedical fields. The simplicity of the unidirectional magnetic fields required to control these miniature robots may offer particular advantages in constrained environments inaccessible with bulky instrumentation.

4. Experimental Section

Thermal Drawing of Elastomer Fibers: To fabricate the preform, SEBS pellets (G 1657 VS, Kraton) were hot pressed in aluminum molds at 140°C for 5 min to mold them into the desired shapes. COCe pellets (Elastomer E-140, TOPAS) were hot pressed between teflon sheets at 125°C for 15 min and cut with razor blades to form bar shapes with different thicknesses of 0.92–2 mm for different COCe composition. Each part was stacked into a channel milled on the PMMA (Extruded acrylic, McMaster–Carr) cladding and hot pressed at 150°C for 1 h to produce a single preform via consolidation (Figure S6, Supporting Information). Using a vertical draw tower, preforms were thermally drawn to 80–320 m long fibers at a temperature range between 225 and 260°C for similar stress conditions (< 200 g mm⁻²). The feed speed of the preform into the furnace was 1 mm min⁻¹ and the drawing speed was 0.40 and 1.60 m min⁻¹ for reduction ratios of 20 and 40, respectively.

Magnetic Composite Synthesis: For $4T_42T_{96}2A_{100}$ polymer, 2,2-Dimethoxy-2-phenyl-acetophenone (1.0 wt%, DMPA, MilliporeSigma), TEGDVE (51.7 wt%, MilliporeSigma), EDDET (44.8 wt%, MilliporeSigma), and PETMP (2.5 wt%, MilliporeSigma) were added in a single vial. DMPA was employed as a photoinitiator to trigger thiol-ene reactions under UV light. The solution was stirred using a vortex mixer for 1.5 min. Then, non-magnetized NdFeB MPs (≈5 µm, MQFP-B-20076-089, Magnequench) were added to the same vial for a 1:2 weight ratio of MPs:polymer matrix and mixed with a vortex mixer for 20 s. This composition corresponds to the maximum concentration of MPs that permits sufficient transmittance of UV light through the polymer matrix to allow the magnetic composite to solidify. All synthetic processes were performed under the red light.

---

to LLD and SLD, respectively. The purple region represents an area where the movement direction is opposite during folding and unfolding motion, therefore the net motion of the walker is ambiguous based on the hybrid statics-dynamics model. c) Distance traveled along the y-direction by the walker depending on foot conditions. Blue and red lines represent LLD and SLD walking motion, respectively. Solid and dashed lines indicate movement of walkers with different and same foot coil conditions, respectively. d) Measured walking velocity along the y-direction dependent on the magnetic field frequency. Blue and red lines represent the mean walking velocities of the LLD and SLD modes, respectively. Shaded areas correspond to the respective standard deviations of walking velocity (n ≥ 5 samples). e) Photographs of a walker used as a cargo carrier. The walker has different foot coil condition. The cargo is marked in yellow. The magnetic fields applied along the z-direction for transporting (left) and releasing (right) modes are plotted under each mode. Scale bar represents 1 cm. f) Photographs of multiple walkers moving along different directions. The walkers have different magnetization and foot coil conditions. The magnetic field oscillates at 2 Hz along the z-direction. Scale bars represent 1 cm. All walker parameters can be found in Table S4 (Supporting Information).

**ADVANCED
SCIENCE NEWS**

www.advancedsciencenews.com

**ADVANCED
MATERIALS**

www.advmat.de

Integration of Magnetic Composite into Fibers: After the preparation of magnetic slurry, the mixture was injected into a microfluidic channel of thermally drawn fibers using a syringe. For stable injection of magnetic composite into microscale fiber channels, one side of the fiber was connected to a piece of tube using UV curable epoxy (NOA68, Norland). After integration of the composite into the fibers, the polymer matrix was immediately exposed to UV light with a wavelength $\lambda = 365$ nm using a UV pen (SpotCure-B6, Kinetic Instruments) and a UV lamp (UVLM-28, UVP) for a duration of 1 and 20 min, respectively. The polymer matrix was photo-cured within 5–10 min of mixing the MPs into the polymer matrix to preserve an even distribution of MPs (Figure S7, Supporting Information).

Characterization of Fibers: For fiber cross-sectional imaging, fiber samples were cut with razor blades after hardening in liquid nitrogen. The images of samples were taken using an optical microscope (AmScope).

An image of NdFeB particles embedded in a polymer matrix was taken using scanning electron microscopy (SEM, Sigma 300 VP, Zeiss).

To confirm ϵ_{max} of fibers and their components, tensile tests were conducted with a mechanical testing machine (20 N load-cell, Zwick/Roell Z2.5). Because the ϵ_{max} of SEBS and COCe could be changed by stress applied during thermal drawing process, their samples were also prepared as thermally drawn fibers with similar stress conditions of < 200 g mm^{-2}. Samples with fiber shape were 1 cm long fibers with cross-sectional area of 0.1 mm^2. The samples for $4T_42T_{96}2A_{100}$ polymer and magnetic composite were molded on Teflon with the dimension as length of 28 mm and cross-sectional area of 3.7 mm^2 because they were not thermally drawn but injected with stress-free condition. A constant stretching speed of 200 mm min^{-1} was applied to all tests. One of the stress–strain curves for each sample was plotted which has the closest ϵ_{max} to average of five samples.

To measure the bending stiffness of six different kinds of magnetic fibers, a dynamic mechanical analyzer (DMA Q800, TA Instruments) was used with a dual cantilever mode. The length of each fiber sample was 6 cm. All measurement was conducted at room temperature with the deformation amplitude of 300 µm. Averages and standard errors were calculated using five samples for each fiber.

For coil diameter–strain curves, the middle part with length of 15 mm of 25 mm long fibers were stretched and relaxed. Averages and standard deviations were measured with D_Cs of five samples with each condition.

Fabrication of 3D Robots via Selective Strain Application: Integrated fibers with a magnetic component were stretched and relaxed to construct helical structure for 3D actuators. For crawlers, 10%COCe fibers with cross-sectional area of 0.1–0.2 mm^2 were prepared with lengths longer than 9 cm. Crawlers were produced using a mechanical testing machine (Zwick/Roell Z2.5) because of their large displacement for transformation of the whole fibers. Applying strain between 250% and 400% resulted in their D_Cs of 0.96–1.22 mm. Total length of crawlers was kept at 18 mm. A self-built stretching setup (Figure S8, Supporting Information) was employed for walkers which could be created with small displacement. Walkers were engineered using longer than 7 cm long 20%COCe fibers with cross-sectional area of 0.5–0.6 mm^2. First, to establish a compact joint helix, the joint coil was fabricated in the middle of fibers by applying 350% strain to the 8.0–10.5 mm long section. A bipedal walker with larger θ_J could be designed with less coiling at the joint by stretching a shorter initial length of linear fiber. Over 350% strain at large fibers easily led to tilted helical structures because of shorter pitch of coils than fiber width. Then each foot coil was formed with distances of 7 and 9 mm from the joint coil at each side. The leg lengths were chosen for minimum feature size in consideration of bending actuation of legs and prevention of overlap of foot coils on alignment fixtures during magnetization. For the foot, 15 or 25 mm long fiber section was stretched with 300% strain to get enough turns of larger coils. After all coiling steps, perversions were removed by rewinding the coils in one direction. For stable standing of bipedal walkers, joint coil and foot coils were arranged with the opposite coiling directions. Here, three coils at both legs or three and four coils at each leg were employed for features with the same or different foot coil conditions, respectively, and remaining fiber parts were cut using razor blades. Stretching and relaxing speeds during all feature fabrication processes were constant as 200 mm min^{-1}.

Magnetization: Fabricated features were magnetized on customized alignment fixtures using an impulse magnetizer (IM-10, ASC Scientific) to get desired magnetic moment directions at each part. The alignment fixtures were designed with diverse geometrical parameters and printed using a 3D printer (Onyx Pro, MarkForged) with carbon-filled nylon. The geometry of alignment fixtures for the crawlers was designed by varying their L_B (0.5–6.5 mm), L_T (0.5–4.5 mm), R_H (1.5–3.5 mm), and R_T (0.5–2.5 mm). An array of alignment fixtures for walkers was designed to vary the $\theta_{M,S}$ (30, 45, and 60°) and the $\theta_{M,L}$ (60, 70, 80, and 90°). Double-sided tape with weak adhesion was used to fix features on alignment fixtures to avoid unwanted strain during detachment. After charging the impulse magnetizer, magnetic fields of over 2.8 T were applied to features for magnetization of NdFeB MPs. One of the advantages of actuators studied in this work was that different magnetic moment directions could be rewritten by re-magnetization with different alignment fixtures.

Magnetic Actuation in an Electromagnetic Coil Setup: To magnetically actuate locomotors using a unidirectional field, a one-axis Helmholtz electromagnetic coil setup was self-built using magnetic wires (20 AWG, SAPT, NEMA MW35C, MWS Wire Industries) (Figure S9, Supporting Information). The setup was powered by a power amplifier (DC-300A II, Crown) and the shape and frequency of the field were controlled using a function generator (33210A, Keysight). Magnetic field strength was measured with a custom probe and an oscilloscope (PicoScope 2204A, Pico Technology). Because of feature sizes of 1–2 cm, their unidirectional locomotion was observed within a 5 cm long stage. In the stage, a uniform magnetic field up to 54.1 mT was applied with a gradient of < 0.7 mT cm^{-1}. For the cargo experiment, a piece of metal wire was employed as a cargo. During all experiments, videos were recorded using smartphone cameras (Galaxy S20, Samsung).

Velocity Measurement: Locomotion velocities were calculated within 3 mm movement of the front foot of the walker or the tail of the crawler at fixed locations of the stage (Figure S9, Supporting Information). The velocities in the plot for relationship between angles and walking direction were measured with 2 Hz regardless of slips. For velocity–frequency plots, averages, and standard deviations were obtained from over five measurements. For each motion under different frequencies, field strength was constant.

Analysis of Walking Modes: A hybrid statics-dynamics model was set to understand walking mode (Supporting Information). Our model assumed that motion was initiated when static equilibrium conditions of either foot of walker were violated under applied magnetic fields. Global motion of the walking robot was predicted using an algorithm implemented in MATLAB r2022b (MathWorks, Natick, MA, USA) which is highlighted in Figure S10 (Supporting Information). For the global direction of walking motion, "folding" and "unfolding" were modeled as discrete phases. We assumed that unfolded walker was in a static equilibrium condition and the condition was again satisfied in its fully folded state by achieving a balance between frictional, elastic, and magnetic loads (Figure S10, Supporting Information). That is, robot was assumed to come to a stop before the direction of the magnetic field reverses. The walking robot was initialized at its natural angle θ_L at the beginning of the folding phase when the magnetic field was turned on. At the beginning of unfolding (when the robot was at its minimal joint angle), the magnetic field decreases, and the spring exerts a torque that acts to open the joint. The re-initialized values for B and θ_J were updated to reflect this (Figure S10, Supporting Information). The algorithm highlighted above was iterated across walking robots with various natural joint and magnetization angles. The sign of the net force was used to determine whether movement was initiated in LLD or SLD mode (Figure 4b; Figures S11 and S12, and Note S2, Supporting Information).

The rotational stiffness of the hinge joint was measured using an electronic balance. The balance was pushed by one leg of walker and the corresponding deflection was measured from videos that were recorded using smartphone cameras.

The coefficient of friction between the walker's foot and the ground was obtained from tanθ where θ was the angle at which walker begins to slip down an inclined plane. A walker was placed on the ground and the ground was tilted until the walker slid. During the experiment, videos were recorded using smartphone cameras to get θ.

2301916 (9 of 11)

Supporting Information

Supporting Information is available from the Wiley Online Library or from the author.

Conflict of Interest

The authors declare no conflict of interest.

Author Contributions

Conceptualization was performed by Y.L. and P.A. Experiments were performed by Y.L., F.K (magnetic actuation in electromagnetic coil setup), G.L. (magnetization fixture fabrication for magnetization), and J.A. (stretching setup). Analyses were performed by Y.L., T.D. (analysis of walking motion), and I.C.G. (velocity calculation). Additional insights into analyses and discussion were provided by A.S., M.J.A., and K.N. X.Z., Y.F., E.T.R., and P.A. supervised the study. Y.L., T.D., F.K. and P.A. wrote the initial manuscript draft. Review and editing was performed by all authors.

Data Availability Statement

The data supporting the findings of this study are available in the manuscript and Supporting Information.

[1] M. Sitti, *Nat. Rev. Mater.* **2018**, *3*, 74.
[2] M. Cianchetti, C. Laschi, A. Menciassi, P. Dario, *Nat. Rev. Mater.* **2018**, *3*, 143.
[3] Z. Shen, F. Chen, X. Zhu, K. T. Yong, G. Gu, *J. Mater. Chem. B* **2020**, *8*, 8972.
[4] R. L. Truby, M. Wehner, A. K. Grosskopf, D. M. Vogt, S. G. M. Uzel, R. J. Wood, J. A. Lewis, *Adv. Mater.* **2018**, *30*, 1706383.
[5] M. Zhu, T. N. Do, E. Hawkes, Y. Visell, *Soft Robot* **2020**, *7*, 179.
[6] B. Jin, H. Song, R. Jiang, J. Song, Q. Zhao, T. Xie, *Sci. Adv.* **2018**, *4*, eaao3865.
[7] Z. Li, N. V. Myung, Y. Yin, *Sci. Robot.* **2021**, *6*, eabi4523.[CrozssRef]
[8] Q. Ge, A. H. Sakhaei, H. Lee, C. K. Dunn, N. X. Fang, M. L. Dunn, *Sci. Rep.* **2016**, *6*, 31110.
[9] M. Kanik, S. Orguc, G. Varnavides, J. Kim, *Science* **2019**, *365*, 145.
[10] Q. He, Z. Wang, Y. Wang, Z. Wang, C. Li, R. Annapooranan, J. Zeng, R. Chen, S. Cai, *Sci. Robot.* **2021**, *6*, eabi9704.
[11] Y. Ohm, C. Pan, M. J. Ford, X. Huang, J. Liao, C. Majidi, *Nat. Electron.* **2021**, *4*, 185.
[12] S. Xu, Y. Chen, N. S. P. Hyun, K. P. Becker, R. J. Wood, *Proc. Natl. Acad. Sci. USA* **2021**, *118*, e2103198118.
[13] S. Wu, W. Hu, Q. Ze, M. Sitti, R. Zhao, *Multifunct. Mater.* **2020**, *3*, 042003.
[14] H. Chung, A. M. Parsons, L. Zheng, *Adv. Intell. Syst.* **2021**, *3*, 2000186.
[15] Y. Kim, X. Zhao, *Chem. Rev.* **2022**, *122*, 5317.
[16] B. J. Nelson, I. K. Kaliakatsos, J. J. Abbott, *Annu. Rev. Biomed. Eng.* **2010**, *12*, 55.
[17] Y. Kim, G. A. Parada, S. Liu, X. Zhao, *Sci. Robot.* **2019**, *4*, eaax7329.
[18] C. Chautems, A. Tonazzini, Q. Boehler, S. H. Jeong, D. Floreano, B. J. Nelson, *Adv. Intell. Syst.* **2020**, *2*, 1900086.
[19] S. Yim, E. Gultepe, D. H. Gracias, M. Sitti, *IEEE Trans. Biomed. Eng.* **2014**, *61*, 513.
[20] D. Son, H. Gilbert, M. Sitti, *Soft Robot.* **2020**, *7*, 10.
[21] S. Yim, M. Sitti, *IEEE Trans. Robot.* **2012**, *28*, 183.
[22] Y. Kim, H. Yuk, R. Zhao, S. A. Chester, X. Zhao, *Nature* **2018**, *558*, 274.
[23] C. Li, G. C. Lau, H. Yuan, A. Aggarwal, V. L. Dominguez, S. Liu, H. Sai, L. C. Palmer, N. A. Sather, T. J. Pearson, D. E. Freedman, P. K. Amiri, M. O. de la Cruz, S. I. Stupp, *Sci. Robot.* **2020**, *5*, eabb9822.
[24] E. Diller, J. Zhuang, G. Zhan Lum, M. R. Edwards, M. Sitti, *Appl. Phys. Lett.* **2014**, *104*, 174101.
[25] G. Z. Lum, Z. Ye, X. Dong, H. Marvi, O. Erin, W. Hu, M. Sitti, *Proc. Natl. Acad. Sci. USA* **2016**, *113*, E6007.
[26] W. Hu, G. Z. Lum, M. Mastrangeli, M. Sitti, *Nature* **2018**, *554*, 81.
[27] J. Kim, S. E. Chung, S. E. Choi, H. Lee, J. Kim, S. Kwon, *Nat. Mater.* **2011**, *10*, 747.
[28] H. W. Huang, M. S. Sakar, A. J. Petruska, S. Pané, B. J. Nelson, *Nat. Commun.* **2016**, *7*, 12263.
[29] T. Xu, J. Zhang, M. Salehizadeh, O. Onaizah, E. Diller, *Sci. Robot.* **2019**, *4*, eaav4494.
[30] E. Diller, M. Sitti, *Adv. Funct. Mater.* **2014**, *24*, 4397.
[31] T. Qiu, T. C. Lee, A. G. Mark, K. I. Morozov, R. Münster, O. Mierka, S. Turek, A. M. Leshansky, P. Fischer, *Nat. Commun.* **2014**, *5*, 5119.
[32] J. Zhang, Z. Ren, W. Hu, R. H. Soon, I. C. Yasa, Z. Liu, M. Sitti, *Sci. Robot.* **2021**, *6*, eabf0112.
[33] S. Lantean, G. Barrera, C. F. Pirri, P. Tiberto, M. Sangermano, I. Roppolo, G. Rizza, *Adv. Mater. Technol.* **2019**, *4*, 1900505.
[34] G. Shao, H. O. T. Ware, L. Li, C. Sun, *Adv. Eng. Mater.* **2020**, *22*, 1900911.
[35] G. Loke, W. Yan, T. Khudiyev, G. Noel, Y. Fink, *Adv. Mater.* **2020**, *32*, 1904911.
[36] C. Lu, S. Park, T. J. Richner, A. Derry, I. Brown, C. Hou, S. Rao, J. Kang, C. T. Mortiz, Y. Fink, P. Anikeeva, *Sci. Adv.* **2017**, *3*, e1600955.
[37] Y. Zhang, X. Li, J. Kim, Y. Tong, E. G. Thompson, S. Jiang, Z. Feng, L. Yu, J. Wang, D. S. Ha, H. Sontheimer, B. N. Johnson, X. Jia, *Adv. Opt. Mater.* **2021**, *9*, 2001815.
[38] J. Hou, Q. Shi, W. Ye, Q. Fan, H. Shi, S. C. Wong, X. Xu, J. Yin, *ACS Appl. Mater. Interfaces* **2014**, *6*, 20868.
[39] M. Bernard, E. Jubeli, M. J. Bakar, L. Tortolano, J. Saunier, N. Yagoubi, *J. Biomed. Mater. Res., Part A* **2017**, *105*, 3333.
[40] D. P. Arnold, N. Wang, *J. Microelectromechan. Syst.* **2009**, *18*, 1255.
[41] T. Saragi, B. Permana, A. Therigan, S. Hidayat, N. Syakir, Risdiana, *Mater. Sci. Forum* **2019**, *966*, 277.

**ADVANCED
SCIENCE NEWS**

www.advancedsciencenews.com

**ADVANCED
MATERIALS**

www.advmat.de

[42] C. Resetco, B. Hendriks, N. Badi, F. D.u Prez, *Mater. Horiz.* **2017**, *4*, 1041.

[43] Q. Li, H. Zhou, C. E. Hoyle, *Polymer* **2009**, *50*, 2237.

[44] C. C. Lee, W. Y. Huang, *Polym. J.* **2011**, *43*, 180.

[45] V. K. Venkiteswaran, L. F. P. Samaniego, J. Sikorski, S. Misra, *IEEE Robot. Autom. Lett.* **2019**, *4*, 1753.

[46] P. Karipoth, A. Christou, A. Pullanchiyodan, R. Dahiya, *Adv. Intell. Syst.* **2021**, *4*, 2100092.

[47] J. Qiao, N. Liu, *Math. Probl. Eng.* **2020**, *2020*, 6701696.

[48] Y. Wang, G. Su, J. Li, Q. Guo, Y. Miao, X. Zhang, *Nano Lett.* **2022**, *22*, 5409.

[49] T. Umedachi, V. Vikas, B. A. Trimmer, presented at *IEEE Int. Conf. on Intelligent Robots and System* Tokyo **2013**, 4590.

[50] A. Leber, C. Dong, R. Chandran, T. D. Gupta, N. Bartolomei, F. Sorin, *Nat. Electron.* **2020**, *3*, 316.

[51] J. S. Marion, N. Gupta, H. Cheung, K. Monir, P. Anikeeva, Y. Fink, *Adv. Mater.* **2022**, *34*, 2201081.

[52] Y. Lee, A. Canales, G. Loke, M. Kanik, Y. Fink, P. Anikeeva, *ACS Cent. Sci.* **2020**, *6*, 2319.

[53] M. Rein, V. D. Favrod, C. Hou, T. Khudiyev, A. Stolyarov, J. Cox, C. C. Chung, C. Chhav, M. Ellis, J. Joannopoulos, Y. Fink, *Nature* **2018**, *560*, 214.